Measuring Temperature Heterogeneities during the Solar-Photothermal Heating Using Quantum Dot Nanothermometry

Journal:	*Analyst*
Manuscript ID	AN-ART-11-2020-002258.R1
Article Type:	Paper
Date Submitted by the Author:	26-Jan-2021
Complete List of Authors:	Loeb, Stephanie; Yale University, Chemical and Environmental Engineering Wei, Haoran; Yale University, Chemical and Environmental Engineering Kim, Jaehong; Yale University, Chemical and Environmental Engineering

Measuring Temperature Heterogeneities during the Solar-Photothermal Heating Using Quantum Dot Nanothermometry

Stephanie K. Loeb[a,b], Haoran Wei[a,c], Jae-Hong Kim[a*]

[a] Department of Chemical and Environmental Engineering and Nanosystems Engineering Research Center for Nanotechnology-Enabled Water Treatment (NEWT), Yale University, 17 Hillhouse Ave, New Haven, Connecticut, USA, 06511

[b] Department of Civil Engineering, McGill University, 817 Rue Sherbrooke Ouest, Montreal, QB, H3A 0C3 Canada

[c] Department of Civil and Environmental Engineering and Environmental Chemistry and Technology Program, University of Wisconsin–Madison, Madison, WI, 53706 USA

Abstract. Small metallic nanoparticles with appropriate surface plasmon resonance frequencies can be extremely efficient absorbers of solar radiation. This efficient absorption can lead to localized heating and highly heterogeneous temperatures. These unique optical properties have inspired research into the development of environmentally relevant solar-to-heat conversion technologies that are based on the light absorption of nanomaterials. The development of robust, reliable, and straight-forward techniques for measuring spatially resolved temperatures in photothermally heated systems can be an indispensable tool to aid future work in this area. Herein, we consider the application of a fluorescent technique that can measure spatially resolved temperatures in solar photothermal systems using CdSe quantum dots (<10 nm diameter). The local temperature of the quantum dot can be determined by monitoring the shift in its fluorescence wavelength resulting from the dilatation of the lattice with increasing temperature. To exploit this property, we fabricated Au nanorod-quantum dot architectures using linkers of varying lengths, and measured the light induced temperature change increasing more rapidly closer to the surface of an Au nanorod. We also compared the effect of Au nanorod coatings and found that silica coating leads to higher overall temperatures compared to organic stabilized Au nanorods.

Introduction

Small metallic nanoparticles are efficient absorbers of photons because of their ability to exhibit a surface plasmon resonance.[1-3] The oscillating electrons generate a local electric field which allows the particle to present an absorption cross-section that is greater than its geometric cross-section.[4] When illuminated with resonant wavelengths in the visible and NIR regions, a part of the absorbed energy is dissipated non-radiatively, leading to a rise in the surface temperature of the nanoparticle.[5] When multiple light-absorbing nanoparticles in close proximity are illuminated simultaneously, they can induce multiple scattering events, increasing photon absorption probability and concentrating light within a small spatial domain.[6-9] Suspensions of photothermal nanoparticles illuminated with concentrated sunlight have achieved highly localized heating, notably permitting steam production after only a few seconds of illumination while bulk water temperatures remained below 10°C.[6] Harnessing these unique optical properties, researchers have been developing a variety of solar photothermal technologies that employ light absorbing nanomaterials to efficiently convert light into usable heat.[10] In particular, several environmentally relevant technologies have been proposed, including water distillation,[11-15] disinfection,[16, 17] sterilization,[18] catalysis,[10, 19] and energy generation applications.[20, 21]

Intrinsically, the temperatures generated in these systems are highly heterogenous. Moreover, the nature of these proposed applications, such as thermal desalination which harnesses a thermal gradient to drive a phase-change from liquid to vapor, are highly dependent on maintaining and controlling an appropriate temperature gradient. Due to the short time scale and the fine spatial resolution desired, there remains a paucity of methods available to accurately measure temperatures in systems that aim to harness nanoparticle-enhanced photothermal heating technologies. The development of robust, reliable, and straight-forward tools for measuring spatially resolved temperatures in photothermally heated systems can play a key role in the future development and optimization of these technologies.

Several methods have been explored to measure temperatures with nanoscale resolution.[22-26] One notable approach involves releasing a thermally sensitive sub-micron probe into the system, wherein the spatial resolution of temperature determination is dependent on the size of the probe and the diffraction limit of light. An ideal probe would have excellent spatial and temperature resolution, the ability to control its location within the sample, and not be sensitive to extraneous factors that may affect the probe response, such as changes in pH, pressure, or background chemical constituents. Quantum dots (QDs) are well known for their ability to fluoresce in different colors when fabricated in different sizes.[27] For example, smaller QDs experience greater exciton confinement which leads to an increase in the effective bandgap of the material.[28] This property has been harnessed for nanoscale temperature measurements by relating the thermally induced dilatation of the QD lattice to the peak wavelength shift observed in its fluorescence spectrum.[29] Dispersions of QDs were first applied as a non-evasive technique to measure physiological temperatures in living cells,[30] and have since also be used to measure higher temperatures above 80 °C.[31] QDs possess many of the characteristics of an ideal nanothermometer, however, questions remain regarding how the spectral response of QDs with changing temperature is effected by external factors, such as organic or inorganic coatings. In particular, the presence of plasmonic nanoparticles has been shown to produce a range of modulations to QD fluorescence including spectral shifts, fluorescent enhancement, or complete fluorescent quenching, depending on the distance between the particles, the excitation and emission wavelengths, and the size and composition of the QD and the plasmonic nanoparticle.[32-35]

Here, we explore the use of QDs to monitor temperature change in systems that have been photothermally heated with simulated solar light. In this study, we aim to establish if a robust and reliable relationship between the fluorescent response of the QD and temperature can be established and examine the effects of the local environment on this relationship. In particular, the proximity of the QD to an on-resonance excited plasmonic nanoparticle will be considered. The use of QDs to measure nanoparticle induced temperature change has been previously reported,[36] however, this study presents their first application for the measurement of temperature heterogeneities in nanoparticle-enhanced solar photothermal systems. Au nanorods (Au NRs) will be used as a candidate plasmonic photothermal nanomaterial, as their photothermal properties have been well characterized, and the ability to tune the surface plasmon resonance peak by adjusting the aspect ratio of the rod permits fine control of its absorption properties. Using cadmium selenide zinc sulfide core-shell QDs (CdSe/ZnS QDs), we observed temperatures increasing more rapidly closer to the surface of a photothermal nanoparticle by attaching QDs to Au NRs with linkers of varying length. We also identified that coating Au NRs in silica led to higher overall temperatures compared to organic stabilized Au NRs. The development of accurate high temperature nanothermometers coupled with the ability to control their location in a given system can provide useful techniques to aid in the future optimization of various photothermal nanoparticle applications.

Materials and Methods

Materials. All reagents for nanoparticle synthesis and functionalization were purchased from Sigma-Aldrich. Gold chloride ($HAuCl_4$, >99.999%) was used as a precursor for the synthesis of Au NRs. Amine functionalized CdSe/ZnS QDs (fluorescence emission at 665 nm) were purchased from Ocean Nanotech as an 8 μM QD particle suspension in phosphate buffer. Heterobifunctional thiol PEG amine derivative (SH-PEG-NH_2; molecular weight 5000) was purchased from NanoCS.

Au NR Synthesis and Surface Modification. Au NRs were synthesized using a seeded-growth method with a cetyltrimethylammonium bromide (CTAB) capping agent as previously reported in the literature.[37-39] Au NRs were quantified and characterized as described previously.[16, 17] Particle number concentrations (particles/mL or nM of nanoparticles) were calculated using the molar mass and density of gold, and an Au NR particle size of 54 nm length and 12 nm width (averaged over 30 particles). CTAB is known to impair the subsequent functionalization of the Au NR surface, and must be removed prior to further processing.[40] Therefore, as a pre-treatment to QD attachment, CTAB was replaced on the Au NR surface with SH-PEG-NH_2 by a tween-assisted stabilization procedure.[41] Aliquots of the as-synthesized Au NRs were pelleted by centrifugation and the supernatant was removed. Small amounts of a concentrated SH-PEG-NH_2 solution were added to the pellet and vortexed thoroughly for 20 s followed by resuspension in 0.01% Tween-20 (v/v) such that the final solution had a concentration of 1, 10, or 100 μM SH-PEG-NH_2. This process was repeated a minimum of 4 times. After the final washing step, PEG functionalized Au NRs (Au NR-PEG) were resuspended in 0.01% Tween-20 to remove excess PEG.

Silica encapsulation of Au NRs was performed using a modified Stöber process.[42] A thin silica layer was deposited onto the Au NR by hydrolysis and condensation of tetraethyl orthosilicate (TEOS). First, 5 mL of as-synthesized Au NRs were washed twice by centrifugation and resuspended in 1 mM CTAB. The pH of the Au NR suspension was adjusted to ~10.5 by dropwise addition of 0.1 M NaOH. TEOS was diluted in anhydrous methanol to make a 10% v/v solution. After rapid and thorough mixing, 50 μL of the TEOS solution was immediately added to the Au NR suspension. The resultant mixture was vortexed briefly, followed by shaking overnight on an orbital shaker.

Fabrication Au NR-QDs Architectures. Three different Au NR-QD architectures were fabricated using Traut's Reagent (2-iminothiolane) as an initiator, which reacts with primary amines to form sulfhydryl groups.[43]

(1) Au NRs functionalized with QDs using 6-amino-1-hexanethiol (AHT) as the linker (Au NR-AHT-QDs): As synthesized Au NRs were twice washed and resuspended in 0.03 M CTAB to reach a final concentration of 0.5 nM Au NRs. 0.5 mg of AHT was added to 3 mL of the Au NR suspension and vortexed for 1 min. Meanwhile, amine-functionalized CdSe/ZnS QDs were added to a freshly prepared solution of 1 mM Traut's Reagent in DI water that had been adjusted to pH ~9.5 by dropwise addition of 0.1 M NaOH. The resultant solution was thoroughly vortexed for 1 min, then left to react for 15 min. The suspension of QDs in Traut's Reagent was then combined with AHT-modified Au NRs (Au NR-AHTs) and vortexed thoroughly for 2 min.

(2) Au NRs functionalized with QDs using SH-PEG-NH_2 as the linker (Au NR-PEG-QDs): QDs were added to a freshly prepared Traut's Reagent solution, mixed, and reacted as described above for Au NR-AHT-QDs. After 15 min, the solution of QDs in Traut's Reagent was combined with 0.5 nM Au NR-PEG-NH_2 and vortexed thoroughly for 2 min.

(3) Silica encapsulated Au NRs functionalized with QDs (Au NR-Si-QDs): Beginning with silica encapsulated Au NRs (Au NR-Si) prepared as described above, 1 mL Au NR-Si was combined with 20 μL of a freshly prepared 5% (v/v) solution of (3-aminopropyl)trimethoxysilane (APTMS) in methanol under vigorous stirring and left to react for 15 min. In the meantime, QDs were added to a freshly prepared solution of 1 mM Traut's Reagent at pH ~9.5 and vortexed thoroughly for 1 min. After 15 min, the suspension of QDs with Traut's Reagent was combined with 0.5 nM Au NR-Si w/APTMS and vortexed thoroughly for 2 min.

Fabricated materials were characterized using an FEI Tecnai Osiris 200kV Transmission Electron Microscope (TEM) and a Varian Cary 50 Bio UV-visible spectrophotometer.

Hydrodynamic radius and zeta potential were determined using dynamic light scattering (DLS) with a NanoBrook Omni Particle Sizer and phase-alternative light scattering (PALS) with a Zeta Potential Analyzer, respectively.

Monitoring Temperature Dependent Fluorescence. Cuvettes containing aqueous suspensions of the different nanoparticle architectures were placed inside a thermostatted cuvette holder (Quantum Northwest) and positioned in the fluorescence monitoring set-up described in **Figure 1a**. Temperature was monitored above and below the optical window using thermocouples (**Figure 1b**). Suspensions were illuminated with simulated sunlight from an ABET industries solar simulator (emission spectra **Figure 1c**) that was passed through a 750 nm longpass filter. The filtered simulated sunlight was passed through a collimating lense and focused using an aspheric condenser to produce a range of intensities. Power density was measured using an Ophir 2A-BB-9 high-sensitivity power sensor with an apeture of 9.5 mm. QD flourescence was activated using a 447 nm diode laser that was positioned through a neutral density filter. Laser power was measured using an Ophir PD300 photodiode sensor. Fluorescence emission was collected through plano-convex lenses and monitored using a Newport C260 UV-vis monochromator with a 500 nm longpass filter at the intake to screen out scattered light from the laser.

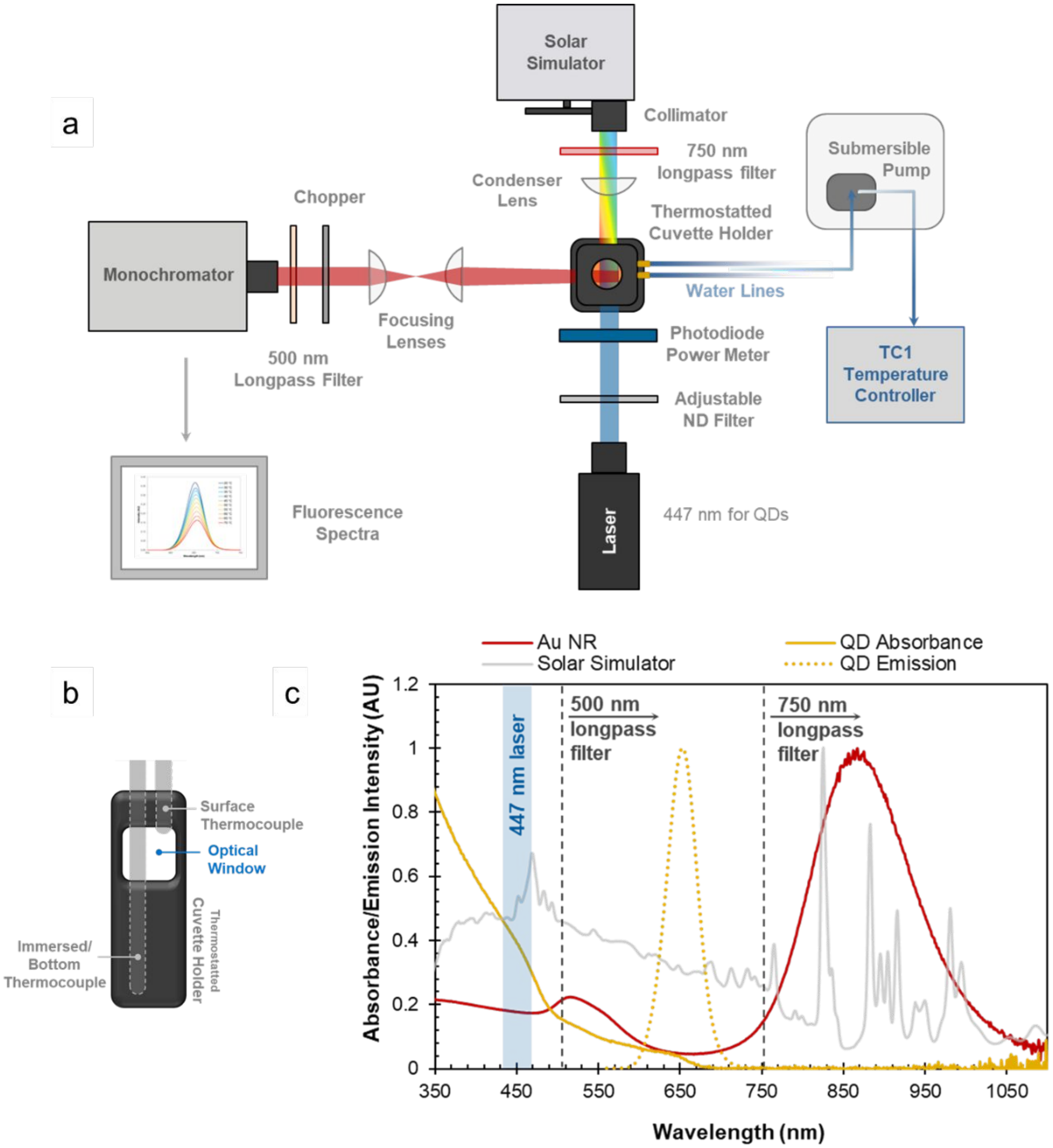

Figure 1. (a) Fluorescence monitoring set-up, (b) Side-view of set-up indicating thermocouple placement (c) Spectral properties of the different materials and light sources used in the study.

Results and Discussion

Fabrication and Characterization of Au NR-QD Architectures. Three different Au NR-QD architectures were fabricated using Traut's Reagent as an initiator, which converts the terminal amine groups on the Au NRs and QDs to sulfhydryl groups.[43] Each fabrication began by functionalizing the surface of the Au NR with amine groups, followed by rapidly combining the

Au NRs with a solution of QDs in Traut's Reagent, leading to dithiol-coupling between the Au NR and the QD (refer to Materials and Methods section for details). The synthesis procedure was performed with low concentrations of Au NRs (0.5 nM) and a relatively high QD:Au NR particle ratio of 5:1 in order to promote QD attachment to the Au NR while minimizing coupling between Au NRs. Schematics of the three structures fabricated are shown in **Figure 2**. Overall, the aim behind fabricating these different Au NR-QD architectures was to test the ability of the QD to report temperature changes at different distances from the photothermal nanoparticle, while maintaining colloidal stability and a strong fluorescence response. Au NRs are an optimal candidate photothermal material for this study because they can be excited on resonance with NIR radiation (longitudinal SPR peak at 875 nm), and these longer wavelengths do not interfere with the excitation/emission spectra of the QDs (**Figure 1c**). In this manner, the Au NR was photothermally heated with simulated solar radiation passed through a 750 nm longpass filter, while the QDs was activated with short flashes of a 447 nm laser and the QD emission spectra was monitored from 600 – 700 nm in order to detect any red-shift in the emission peak due to increasing temperatures.

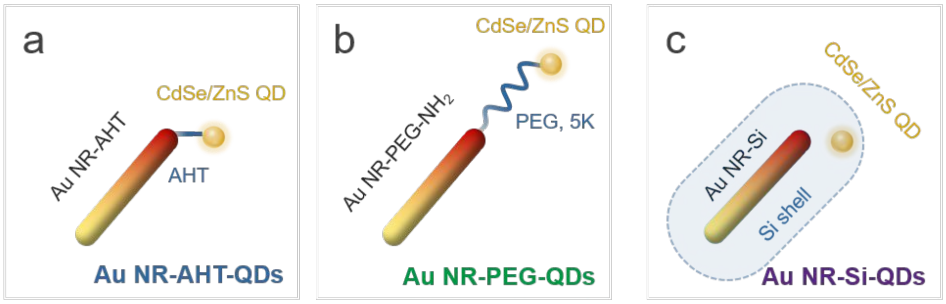

Figure 2. Schematic of different Au NR-QD architectures fabricated in this study. (a) Au NR-AHT-QDs; (b) Au NR-PEG-QDs; and (c) Au NR-Si-QDs

UV-vis measurements taken throughout the fabrication of each Au NR-QD architecture confirm their stability, as indicated by the negligible broadening of the longitudinal SPR band at 875 nm. Au NR-AHT-QDs were the most challenging structure to fabricate since Au NR-AHT is not stable in aqueous suspension, likely because the short-chain amine-hexane molecule does not provide enough charge repulsion or steric hinderance to prevent aggregation between Au NRs. Once AHT was added to the Au NR-CTAB suspension, UV-vis time-series measurements

(**Figure 3a**) showed a slow broadening of the SPR peak as surface-bound CTAB was gradually replaced with AHT. If left to react overnight, Au NR-AHT will continue to aggregate, eventually turning the solution transparent and irreversibly eliminating the SPR band. However, when the mixture of QDs in Traut's Reagent is added, dithiol coupling between AHT and the QDs stabilizes the structures, preventing further aggregation. Au NR-AHT-QD suspensions were stable in aqueous suspension and could be stored for several weeks. The ideal reaction time for QD-Au NR coupling was determined to be 10 minutes, which resulted in minimal aggregation while still showing efficient attachment of QDs to the Au NR (TEM images in **Figure 4b**).

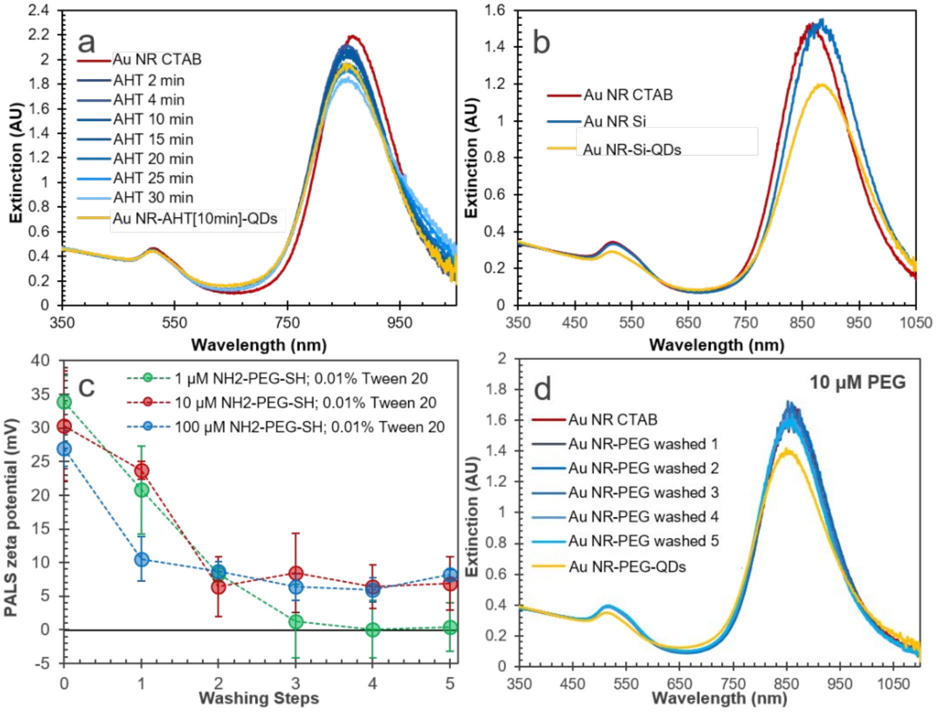

Figure 3. Characterization of Au NR-QDs throughout fabrication. (a) UV-Vis measurements showing the replacement of CTAB with AHT before and after mixing with QDs in Traut's Reagent (Au NR-AHT-QDs); (b) UV-Vis measurements of Au NRs after deposition of a thin silica layer (Au NR-Si) and after reacting with APTMS and QDs (Au NR-Si-QDs); (c) zeta potential measurements after repeated incubation, washing, and re-suspension of Au NRs in a solution of 1-100 µM SH-PEG-NH_2 with 0.01% Tween 20; and (d) UV-vis spectra showing the stability of the Au NR-PEG after repeated washing steps and after reacting with QDs in Traut's Reagent.

Both Au NR-Si and Au NR-PEG are stable structures that can be prepared ahead of time and stored, permitting easier QD functionalization. Complete removal of CTAB and replacement with SH-PEG-NH_2 was achieved using a Tween-assisted PEG exchange method,[41] as shown in **Figure 3c-d**. Repeated incubation, washing, and re-suspension of Au NRs in a solution of 1-100 μM SH-PEG-NH_2 with 0.01% Tween 20 was able to reduce the surface charge on the Au NR to 5-10 mV after 4 washing steps. The terminal amine group should leave the Au NR surface with a weak positive charge, therefore 10 μM SH-PEG-NH_2 with 4 washing steps was selected as the best concentration for processing further samples in this study. Little to no aggregation was detected during PEG functionalization or after reacting with the mixture of QDs in Traut's Reagent (**Figure 3d**). During Au NR-Si fabrication, a thin shell of silica was deposited around the Au NR by hydrolysis and condensation of TEOS and was confirmed by the characteristic red-shift of the peak SPR band,[42] shown in **Figure 3b**. Several methods were tested to attach QDs to the Au NR-Si (described in the supporting information), however, the most successful was a co-condensation approach, in which a small amount of APMTS was added to the Au NR-Si suspension to further grow the silica shell followed quickly by the addition of the QDs in Traut's Reagent. This resulted in the QDs being incorporated into the additional layers of silica shell.

TEM images of the pristine Au NRs along with each Au NR-QD architecture are shown in **Figure 4a-d**. The average number of QDs per Au NR for each structure was determined by visually examining a minimum of 15 nanoparticles in TEM images. Only individual particles that did not overlap with neighbors in these images were included in the analysis to prevent double counting of QDs. Au NR-AHT-QDs had the highest attachment efficiency at 3.8 ± 1.4 QDs per Au NR, followed by Au NR-Si-QDs at 2.1 ± 1.3 QDs per Au NR, and lastly Au NR-PEG-QDs at 1.8 ± 1.7 QDs per Au NR. During the synthesis procedure, a ratio of 1:5 Au NRs to QDs was used for each sample, therefore a significant fraction of the QDs remained free in solution. These background QDs were impractical to remove, as the Au NR-QDs were not robust enough to be purified by centrifugation.

DLS measurements of hydrodynamic radius taken before and after QD functionalization showed a small increase in particle size after QD attachment for each architecture (**Figure 4e**). These results provide important additional support for the successful fabrication of the desired structures and their stability in aqueous suspension. The drying steps in TEM sample preparation can lead to non-uniform deposition and aggregation (drying effects), whereas UV-vis and light scattering measurements preserve the true unaltered colloidal state of the suspension. Fluorescence measurements (447 nm excitation, **Figure 4f**) comparing the relative intensity of each structure showed different responses for the QDs once functionalized to the Au NRs. These fluorescent measurements correspond with the UV-vis spectra shown as yellow curves in **Figures 3a, b, and d**. The local interaction between QDs and plasmonic nanoparticles has been reported to produce a range of responses, from fluorescent enhancement to complete fluorescent quenching, depending on the distance, excitation wavelengths, and the size and composition of the QD and the plasmonic nanoparticle.[32-34] In our study, the fluorescence intensity was the lowest for the Au NR-AHT-QD sample, consistent with TEM images indicating a close proximity of the QDs to the Au NRs (**Figure 4b**). However, as noted in **Figure 3a**, an initial broadening of the SPR band was detected during the fabrication of Au NR-AHT, indicating some aggregation of the Au NRs prior to functionalization with the QDs. If this aggregation also led to an increased coupling between QDs, it could contribute to the decrease in fluorescence intensity observed in the Au NR-AHT-QD sample. Fluorescence intensities for the Au NR-PEG-QD and Au NR-Si-QD samples were slightly higher than the Au NR-AHT-QDs, although lower than the samples containing only QDs, or an unreacted mixture of Au NR-CTAB and QDs. This is consistent with the larger distances between the Au NRs and the QDs observed in **Figure 4c-d**.

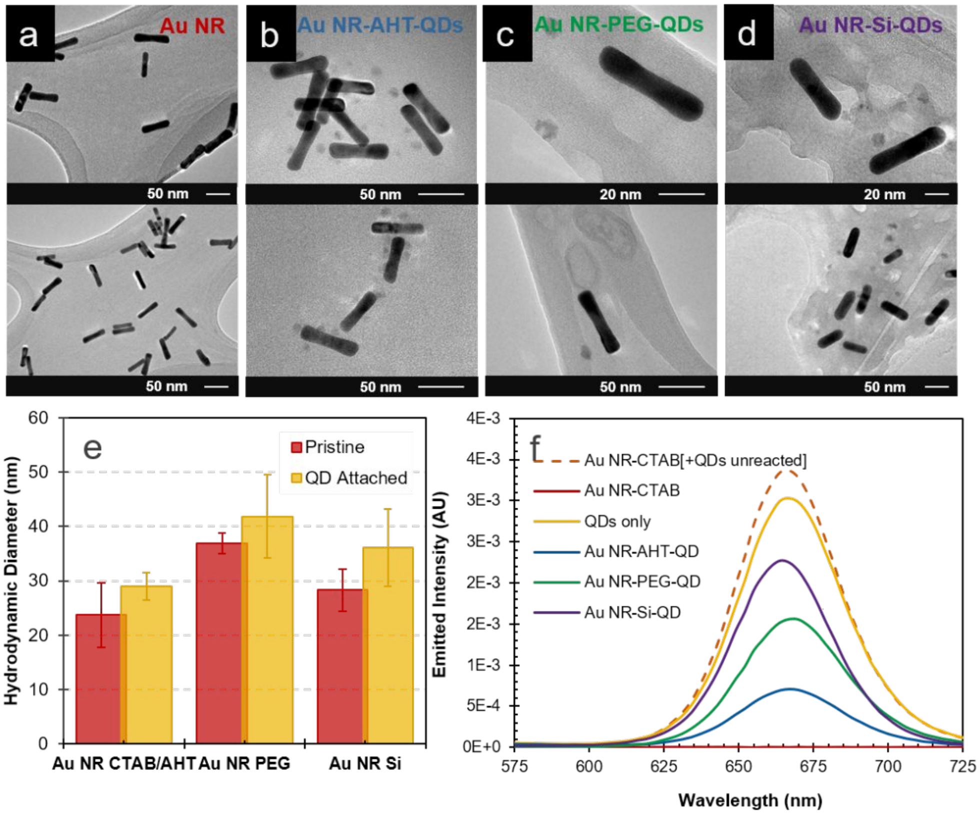

Figure 4. Characterization of Au NR-QD architectures. TEM images of (a) pristine Au NR; (b) Au NR-AHT-QDs; (c) Au NR-PEG-QDs; (d) Au NR-Si-QDs; (f) DLS measurements of hydrodynamic radius before and after QD attachment; and (f) comparative fluorescence emission intensity from each structure.

Temperature Dependent Fluorescence. In order to relate changes in the QD emission spectra to changes in temperature, a reliable and predictable relationship between the two must be established. An increase in temperature is known to induce both a red-shift in wavelength and a decrease in fluorescence intensity for CdSe/ZnS QDs.[27] However, the presence of plasmonic nanoparticles has also been shown to modulate the intensity of fluorophores, including QDs.[32-34, 43-45] To relate QD spectral changes to temperature, a calibration for each Au NR-QD sample was developed by ramping up the temperature of a thermostatted cuvette, as shown for each material in **Figure 5**. Firstly, it was noted that although the change in fluorescence intensity with temperature varied smoothly between the different structures fabricated, it also varied widely between sample batches. As such, monitoring changes in QD intensity did not prove to be a reliable method for relating the QD spectrum to changes in temperature. Alternatively, peak wavelength shift was found to reliably and consistently respond to changes in temperature. The peak of each curve was determined by fitting a polynomial from 645-690 nm and extracting the maximum value. This was found to be far more accurate than simply extracting the wavelength value that corresponded to the absolute maximum intensity reported, as it allowed the measurement to be taken quickly using a much larger scan interval (3 nm). Over three trials, the average slope of the calibration for QDs only was 0.15 ± 0.01 nm/°C, while for Au NR-AHT-QDs it was 0.12 ± 0.01 nm/°C, for Au NR-PEG-QDs it was 0.12 ± 0.01 nm/°C, and finally for Au NR-Si-QDs it was 0.13 ± 0.02 nm/°C. All fits demonstrated high linearity with $R^2 > 0.99$. Although the difference between the reported slopes for different samples was small, the slope of the QD only calibration was consistently larger than for the samples containing Au NRs. This indicates that aspects of the local environment of the QD, such as the presence of an organic (AHT, PEG) or inorganic (Si) coatings and the proximity to plasmonic nanoparticles, likely influenced the ability of temperature changes to expand the QD lattice. The variation in peak wavelength shift was far less than the observed variation for changes in fluorescent intensity with temperature.

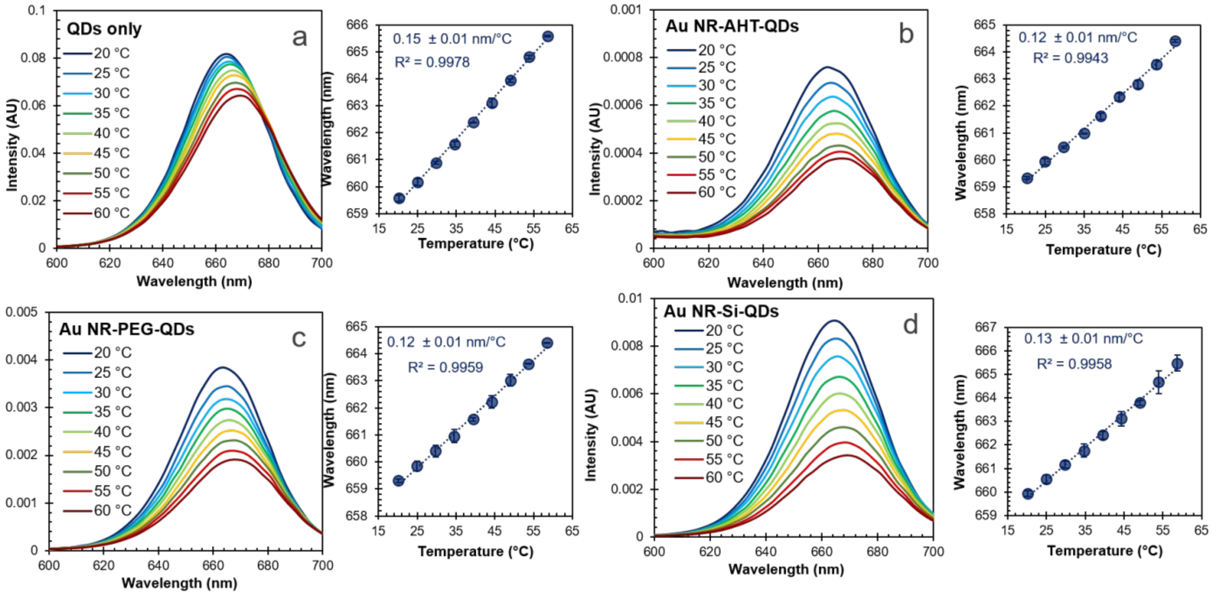

Figure 5. QD temperature calibrations for each Au NR-QD architecture. (a) QDs only; (b) Au NR-AHT-QDs; (c) Au NR-PEG-QDs; and (d) Au NR-Si-QDs. Spectral curves represent an example calibration, while the line graphs present an average of three trials, with error bars showing a 95% confidence interval.

The ability of the QDs to measure temperature increase in a photothermally heated system was validated by illuminating cuvettes containing suspensions of each different Au NR-QD architecture with 2 Sun illumination from a solar simulator passed through a 750 nm longpass filter. This filter allows us to retain the portion of the spectrum that excites the Au NRs along its longitudinal SPR band, while filtering out light that would interfere with the excitation/emission wavelength of the QDs. Samples were not stirred, so temperature heterogeneities between the surface of the sample (2 cm above the illumination window) and bottom of the cuvette were anticipated. We established the boundaries of this heterogeneity throughout the illumination period by measuring temperature in the cuvette with a thermocouple placed at the surface of the cuvette and also with a thermocouple fully immersed in the solution touching the bottom of the cuvette (as depicted in **Figure 1b**). **Figure 6** shows these temperature traces, along with the temperature response calculated from measuring the QD fluorescence.

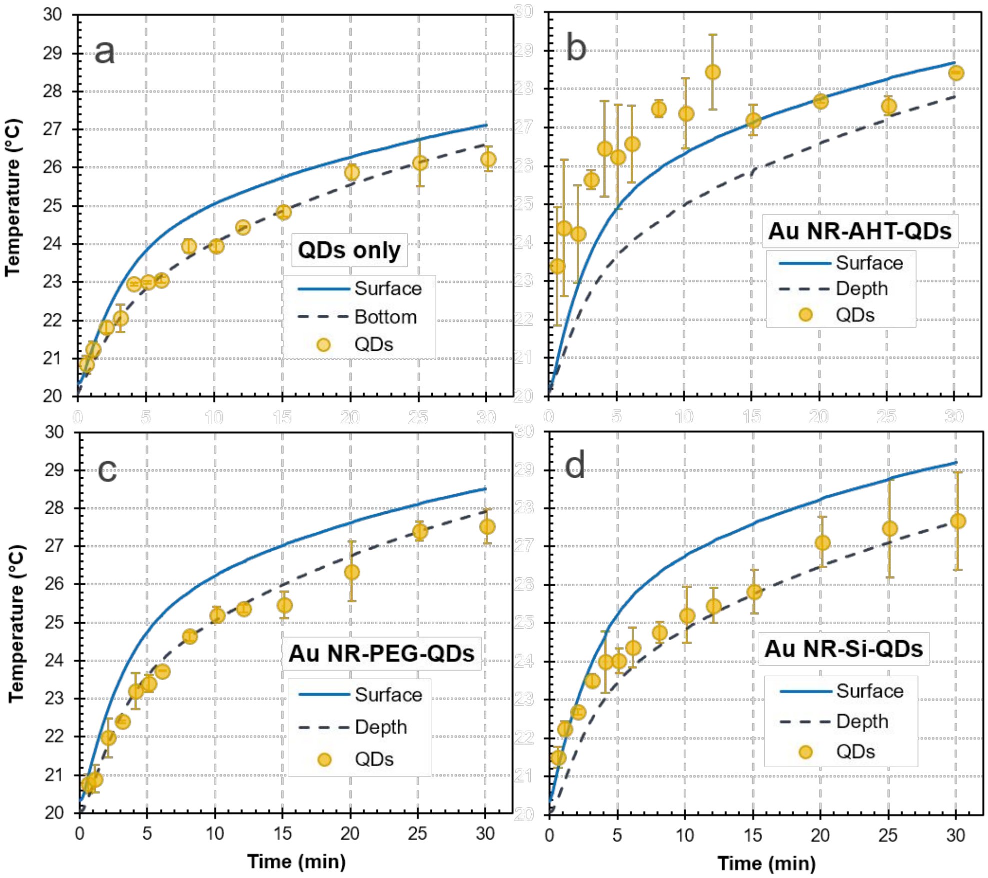

Figure 6. Photothermal induced heating under 2 Sun illumination measured using a thermocouple placed at the very surface of the cuvette (surface; light blue line), fully immersed in the solution touching the bottom of the cuvette (depth; dashed dark blue line), and determined using QD fluorescence (yellow circles) for (a) QDs only; (b) Au NR-AHT-QDs; (c) Au NR-PEG-QDs; and (d) Au NR-Si-QDs.

According to the thermocouple trace, all samples containing Au NRs reached higher temperatures than the control sample (containing only QDs), with Au NR-AHT-QDs and Au NR-PEG-QDs reaching nearly the same maximum temperature of ~28.5 °C, while samples containing suspensions of Au NR-Si-QDs were able to achieve temperatures above 29 °C. The ability of silica coated NRs to achieve overall higher temperatures is likely due to their increased light scattering, increasing light concentration and absorption. Differences in silica coating thickness were not considered in this study. Further investigation of the impact of silica shell thickness on temperature and light scattering is recommended and may yield greater insights. QD measurements proved to be repeatable over several trials, with the control sample measurements aligning very closely with the measurements from the thermocouple immersed completely into the cuvette (**Figure 6a**). This was likewise true for the Au NR-PEG-QDs sample (**Figure 6c)** which very closely matched to the fully immersed thermocouple temperature trace. However, for the Au NR-AHT-QD and Au NR-Si-QD samples, QDs reported a temperature higher than the fully immersed thermocouple, particularly for the first 10 minutes, with Au NR-Si-QDs reporting an average of 0.8 ± 0.4 °C higher, and Au NR-AHT-QDs reporting an average of 2.5 ± 0.4 °C higher than the depth thermocouple trace for the first 10 time points. Indeed, for the Au NR-AHT-QDs, the QDs reported temperatures of 1.7 ± 0.6 °C higher than the surface thermocouple tracer for the first 10 time points. Only the first two time points (up to 1 min heating) for the Au NR-Si-QD sample reported temperatures higher than the surface thermocouple trace. For both Au NR-AHT-QDs and Au NR-Si-QDs, these differences decreased over the illumination time period as the temperature began to plateau and the samples approached equilibrium.

These results demonstrate the ability of the QDs to measure temperature heterogeneities in photothermally heated systems that cannot be detected using traditional temperature measurement techniques, such as a thermocouple. According to the QD response, initial photothermal heating near the nanoparticles in the illumination window is in a non-equilibrium condition with the solution above and below, however, due to the significant fraction of free QDs in solution, we must recognize that the temperature results represent an average of many different distances from the nanoparticle. In this manner, each Au NR-QD architecture fabricated in this study has a set minimum possible distance between the QD and the Au NR determined by the type of linker. QD temperature measurements shortly after the start of illumination were higher for architectures with shorter linkers and greater attachment efficiencies. Although these results indicate the potential for using QDs in solar photothermally heated systems, overall temperature increase was minimal due to the low power density of the light source and the low concentrations of nanoparticles used in this study. The ability of QDs to report temperature based on spectral shift rather than intensity was integral to their success, since many factors, including the resonant excitation of the photothermal nanoparticle, can have a large impact on the fluorescence intensity. The ability to control the location of the QD within the system and report the temperatures at different average distances from the photothermal materials has the potential to provide highly valuable information for the future development and design of materials for environmentally relevant applications of photothermal nanoparticles.

Associated Content

Supporting Information. Additional material available in the Supporting Information as cross-referenced throughout. This material is available free of charge via the Internet at XXX

Author Information

Corresponding Author. E-mail: jaehong.kim@yale.edu. Tel: +1-203-432-4386

Note. The authors declare no competing financial interest.

Author Contributions. J.H.K. and S.K.L designed research; H.W. and S.K.L. performed research; S.K.L. and H.W. analyzed data; and S.K.L. and J.H.K. wrote the paper.

Acknowledgements. This work was partly supported by the NSF Nanosystems Engineering Research Center for Nanotechnology-Enabled Water Treatment (EEC-1449500).

References

1. N. J. Halas, S. Lal, W. S. Chang, S. Link and P. Nordlander, *Chem. Rev.*, 2011, **111**, 3913-3961.
2. S. Eustis and M. A. El-Sayed, *Chem. Soc. Rev.*, 2006, **35**, 209-217.
3. A. Naldoni, V. M. Shalaev and M. L. Brongersma, *Science*, 2017, **356**, 908-909.
4. C. F. Bohren, *Am. J. Phys.*, 1983, **51**, 323-327.
5. M. L. Brongersma, N. J. Halas and P. Nordlander, *Nat. Nanotechnol.*, 2015, **10**, 25-34.
6. O. Neumann, A. S. Urban, J. Day, S. Lal, P. Nordlander and N. J. Halas, *ACS Nano*, 2013, **7**, 42-49.
7. N. J. Hogan, A. S. Urban, C. Ayala-Orozco, A. Pimpinelli, P. Nordlander and N. J. Halas, *Nano Lett.*, 2014, **14**, 4640-4645.
8. M. Gao, L. Zhu, C. K. Peh and G. W. Ho, *Energy Environ. Sci.*, 2019, **12**, 841-864.
9. S. Baral, A. J. Green, M. Y. Livshits, A. O. Govorov and H. H. Richardson, *ACS Nano*, 2014, **8**, 1439-1448.
10. L. Zhu, M. Gao, C. K. N. Peh and G. W. Ho, *Mater. Horiz.*, 2018, **5**, 323-343.
11. P. D. Dongare, A. Alabastri, S. Pedersen, K. R. Zodrow, N. J. Hogan, O. Neumann, J. Wu, T. Wang, A. Deshmukh, M. Elimelech, Q. Li, P. Nordlander and N. J. Halas, *Proc. Natl. Acad. Sci. U.S.A*, 2017, **114**, 6936-6941.
12. A. Politano, P. Argurio, G. Di Profio, V. Sanna, A. Cupolillo, S. Chakraborty, H. A. Arafat and E. Curcio, *Adv. Mater.*, 2017, **29**, 1603504.
13. J. Wu, K. R. Zodrow, P. B. Szemraj and Q. Li, *J. Mater. Chem. A*, 2017, **5**, 23712-23719.
14. P. Wang, *Environ. Sci.: Nano*, 2018, **5**, 1078-1089.
15. L. Zhou, Y. L. Tan, J. Y. Wang, W. C. Xu, Y. Yuan, W. S. Cai, S. N. Zhu and J. Zhu, *Nat. Photonics*, 2016, **10**, 393-399.
16. S. Loeb, C. Li and J. H. Kim, *Environ. Sci. Technol.*, 2018, **52**, 205-213.
17. S. K. Loeb, J. Kim, C. Jiang, L. S. Early, H. Wei, Q. Li and J.-H. Kim, *Environ. Sci. Technol.*, 2019, **53**, 7621-7631.
18. O. Neumann, C. Feronti, A. D. Neumann, A. Dong, K. Schell, B. Lu, E. Kim, M. Quinn, S. Thompson and N. Grady, *Proc. Natl. Acad. Sci. U. S. A.*, 2013, **110**, 11677-11681.
19. H. Wei, S. K. Loeb, N. J. Halas and J. H. Kim, *Proc. Natl. Acad. Sci. U.S.A*, 2020, **117**, 15473.

20. M. Gao, C. K. Peh, H. T. Phan, L. Zhu and G. W. Ho, *Adv. Energy Mater.*, 2018, **8**, 1800711.

21. L. Zhu, M. Gao, C. K. N. Peh, X. Wang and G. W. Ho, *Adv. Energy Mater.*, 2018, **8**, 1702149.

22. P. Neumann, I. Jakobi, F. Dolde, C. Burk, R. Reuter, G. Waldherr, J. Honert, T. Wolf, A. Brunner, J. H. Shim, D. Suter, H. Sumiya, J. Isoya and J. Wrachtrup, *Nano Lett.*, 2013, **13**, 2738-2742.

23. G. Kucsko, P. C. Maurer, N. Y. Yao, M. Kubo, H. J. Noh, P. K. Lo, H. Park and M. D. Lukin, *Nature*, 2013, **500**, 54-58.

24. C. D. S. Brites, P. P. Lima, N. J. O. Silva, A. Millán, V. S. Amaral, F. Palacio and L. D. Carlos, *J. Lumin.*, 2013, **133**, 230-232.

25. L. H. Fischer, G. S. Harms and O. S. Wolfbeis, *Angew. Chem., Int. Ed*, 2011, **50**, 4546-4551.

26. J. S. Donner, S. A. Thompson, M. P. Kreuzer, G. Baffou and R. Quidant, *Nano Lett.*, 2012, **12**, 2107-2111.

27. L. M. Maestro, E. M. Rodriguez, F. S. Rodriguez, M. C. la Cruz, A. Juarranz, R. Naccache, F. Vetrone, D. Jaque, J. A. Capobianco and J. G. Sole, *Nano Lett.*, 2010, **10**, 5109-5115.

28. B. O. Dabbousi, J. Rodriguez-Viejo, F. V. Mikulec, J. R. Heine, H. Mattoussi, R. Ober, K. F. Jensen and M. G. Bawendi, *J. Phys. Chem. B*, 1997, **101**, 9463-9475.

29. S. Li, K. Zhang, J. M. Yang, L. Lin and H. Yang, *Nano Lett.*, 2007, **7**, 3102-3105.

30. J. M. Yang, H. Yang and L. Lin, *ACS Nano*, 2011, **5**, 5067-5071.

31. Y. Y. Li and B. Q. Li, *RSC Advances*, 2014, **4**, 24612-24618.

32. T. Pons, I. L. Medintz, K. E. Sapsford, S. Higashiya, A. F. Grimes, D. S. English and H. Mattoussi, *Nano Lett.*, 2007, **7**, 3157-3164.

33. R. Wargnier, A. V. Baranov, V. G. Maslov, V. Stsiapura, M. Artemyev, M. Pluot, A. Sukhanova and I. Nabiev, *Nano Lett.*, 2004, **4**, 451-457.

34. B. Nikoobakht, C. Burda, M. Braun, M. Hun and M. A. El-Sayed, *Photochem. Photobio.l*, 2002, **75**, 591-597.

35. G. F. Zhang, Y. G. Peng, H. Q. Xie, B. Li, Z. J. Li, C. G. Yang, W. L. Guo, C. B. Qin, R. Y. Chen, Y. Gao, Y. J. Zheng, L. T. Xiao and S. T. Jia, *Front. Phys.*, 2018, **14**, 23605.

36. L. M. Maestro, P. Haro-Gonzalez, A. Sanchez-Iglesias, L. M. Liz-Marzan, J. Garcia Sole and D. Jaque, *Langmuir*, 2014, **30**, 1650-1658.

37. W. Ni, X. Kou, Z. Yang and J. Wang, *ACS Nano*, 2008, **2**, 677-686.

38. Z. Sun, Z. Yang, J. Zhou, M. H. Yeung, W. Ni, H. Wu and J. Wang, *Angew. Chem., Int. Ed*., 2009, **48**, 2881-2885.

39. B. Nikoobakht and M. A. El-Sayed, *Chem. Mater.*, 2003, **15**, 1957-1962.

40. M. R. Jones, R. J. Macfarlane, B. Lee, J. Zhang, K. L. Young, A. J. Senesi and C. A. Mirkin, *Nat. Mater.*, 2010, **9**, 913-917.

41. J. Li, B. Zhu, Z. Zhu, Y. Zhang, X. Yao, S. Tu, R. Liu, S. Jia and C. J. Yang, *Langmuir*, 2015, **31**, 7869-7876.

42. L. R. Rowe, B. S. Chapman and J. B. Tracy, *Chem. Mater*, 2018, **30**, 6249-6258.

43. D. Nepal, L. F. Drummy, S. Biswas, K. Park and R. A. Vaia, *ACS Nano*, 2013, **7**, 9064-9074.

44. Y. Xia, L. Song and C. Zhu, *Anal. Chem.*, 2011, **83**, 1401-1407.

45. Q. Wu, L. Chen, L. Huang, J. Wang, J. Liu, C. Hu and H. Han, *Biosens. Bioelectron.*, 2015, **74**, 16-23.